

Holograms for acoustics

Kai Melde¹, Andrew G. Mark¹, Tian Qiu¹ & Peer Fischer^{1,2}

Holographic techniques are fundamental to applications such as volumetric displays¹, high-density data storage and optical tweezers that require spatial control of intricate optical² or acoustic fields^{3,4} within a three-dimensional volume. The basis of holography is spatial storage of the phase and/or amplitude profile of the desired wavefront^{5,6} in a manner that allows that wavefront to be reconstructed by interference when the hologram is illuminated with a suitable coherent source. Modern computer-generated holography⁷ skips the process of recording a hologram from a physical scene, and instead calculates the required phase profile before rendering it for reconstruction. In ultrasound applications, the phase profile is typically generated by discrete and independently driven ultrasound sources^{3,4,8–12}; however, these can only be used in small numbers, which limits the complexity or degrees of freedom that can be attained in the wavefront. Here we introduce monolithic acoustic holograms, which can reconstruct diffraction-limited acoustic pressure fields and thus arbitrary ultrasound beams. We use

rapid fabrication to craft the holograms and achieve reconstruction degrees of freedom two orders of magnitude higher than commercial phased array sources. The technique is inexpensive, appropriate for both transmission and reflection elements, and scales well to higher information content, larger aperture size and higher power. The complex three-dimensional pressure and phase distributions produced by these acoustic holograms allow us to demonstrate new approaches to controlled ultrasonic manipulation of solids in water, and of liquids and solids in air. We expect that acoustic holograms will enable new capabilities in beam-steering and the contactless transfer of power, improve medical imaging, and drive new applications of ultrasound.

The complexity of a wavefront is typically characterized by its information content, quantified by the scalar space-bandwidth product, SW (ref. 13). Because this is invariant, a transmission hologram's SW limits the intricacy of the acoustic field in the workspace downstream from it, down to the diffraction limit (see Methods). In a digital hologram

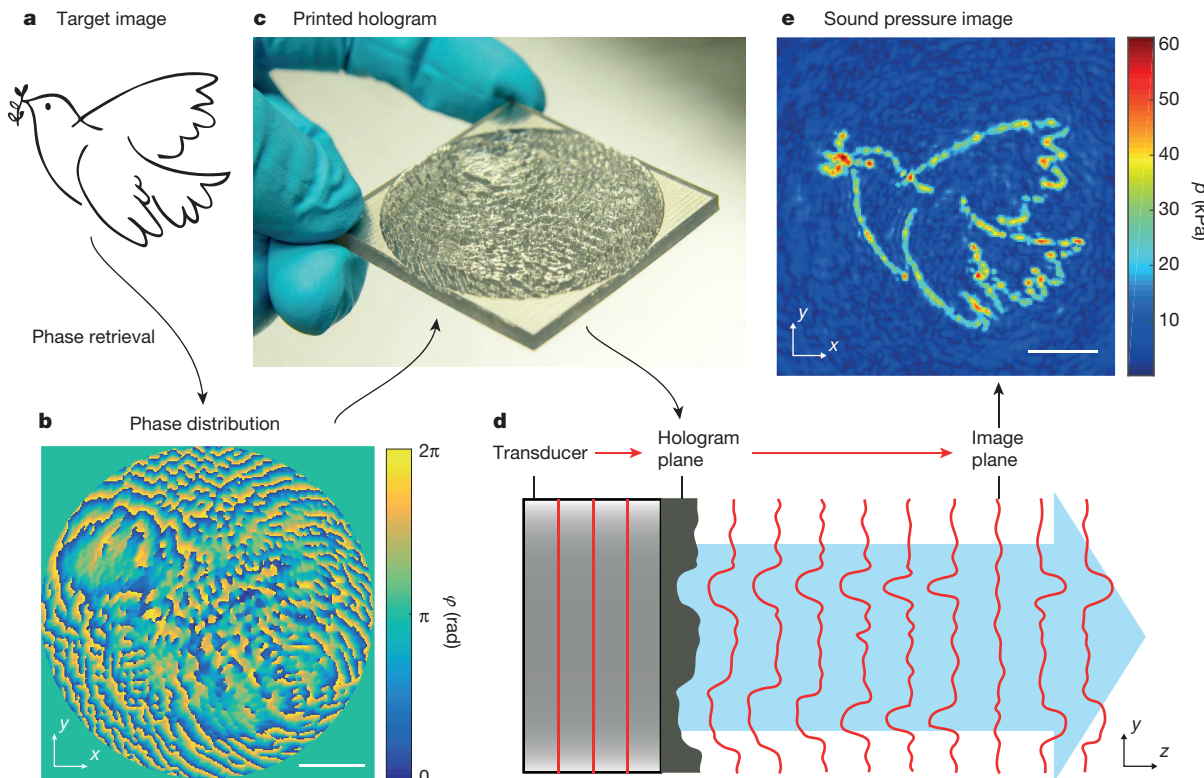


Figure 1 | Workflow for generating and reconstructing arbitrary acoustic images. **a**, Target image amplitude used as input to the iterative angular spectrum approach (IASA). **b**, Computed phase (ϕ) distribution for 2.06 MHz ultrasound (scale bar, 10 mm). **c**, The 3D printed transmission hologram (50 mm side length). The topography of the hologram surface encodes the desired phase information. **d**, The hologram

converts a planar wavefront from the transducer into the required phase distribution. This travelling wave diffracts to form an image in the image plane. **e**, Scanned hydrophone pressure (p) measurement in the image plane showing the reconstructed target image (scale bar, 10 mm). See Methods for details of measurements.

¹Max Planck Institute for Intelligent Systems, Heisenbergstrasse 3, 70569 Stuttgart, Germany. ²Institute for Physical Chemistry, University of Stuttgart, Pfaffenwaldring 55, 70569 Stuttgart, Germany.

consisting of $N \times N$ pixels, the space-bandwidth product is given by $SW = N^2$ (ref. 14). Thus the information content of the acoustic field depends directly on the number of pixels that can be independently addressed in the hologram that generates it. Qualitatively, holograms with higher SW lead to reconstructions with larger spatial extent and finer detail.

Currently, the dominant method for manipulating acoustic wavefronts is to use phased array transducers (PATs), in which each pixel is addressed by an independent transducer with controllable phase and amplitude^{3,4,8}. The distinct advantage of PATs is that they are dynamic and can be reconfigured in real time. However, they typically require elaborate arrays in which each transducer is individually addressable, together with the support electronics to independently drive and synchronize each of those transducers. Thus the complexity and cost of PATs scale unfavourably with larger pixel counts and higher information content. These difficulties have encouraged strategies for minimizing the number of active elements through techniques such as sparsely populated arrays and element multiplexing⁸. Although these simplify system design, they further limit the attainable information content.

Our approach is to introduce a monolithic acoustic hologram—the acoustic analogue of the optical kinoform¹⁵. Placed in the path of the ultrasound wave, it modifies the output of a single ultrasonic transducer to generate a designed 2D phase profile. It allows us to create 3D sound fields with diffraction-limited resolution, using a simple planar transducer driven by a single function generator and amplifier. Figure 1

illustrates the scheme we use to generate arbitrary sound pressure fields with the acoustic hologram. We start by defining the desired 2D acoustic field (that is, the image) and the plane where it will appear. In this case the image is a circular area 50 mm in diameter consisting of a binary amplitude map with unrestricted phase at a distance 30 mm from the hologram plane (Fig. 1a). We use an iterative angular spectrum approach (IASA) adapted from optical holography¹⁶ to compute the phase map of the acoustic hologram (see Methods for further details). That phase map (Fig. 1b) is rendered into a 3D-printed transmission element whose material has a speed of sound different from the surrounding medium ('printed hologram', Fig. 1c). In fabricating the hologram, we assume 1D propagation inside the thin element and neglect shear waves and attenuation, so that the phase lag of each pixel of the hologram is proportional to its thickness (see Extended Data Fig. 1 for examples of profile scans). In the reconstruction process (Fig. 1d) a travelling plane wave passes through the hologram, emerges with the required phase distribution, diffracts to form a real image at the desired plane, and propagates further. Figure 1e shows the high-resolution ultrasound image projected in water by the hologram. Comparison with the calculated forward propagated sound field (Extended Data Fig. 2) indicates that the few defects present arise from the hologram optimization.

Because the hologram is fabricated by 3D printing, its SW is limited only by the printer's build size and resolution. The hologram in Fig. 1c is computed for 2 MHz excitation, a frequency common in

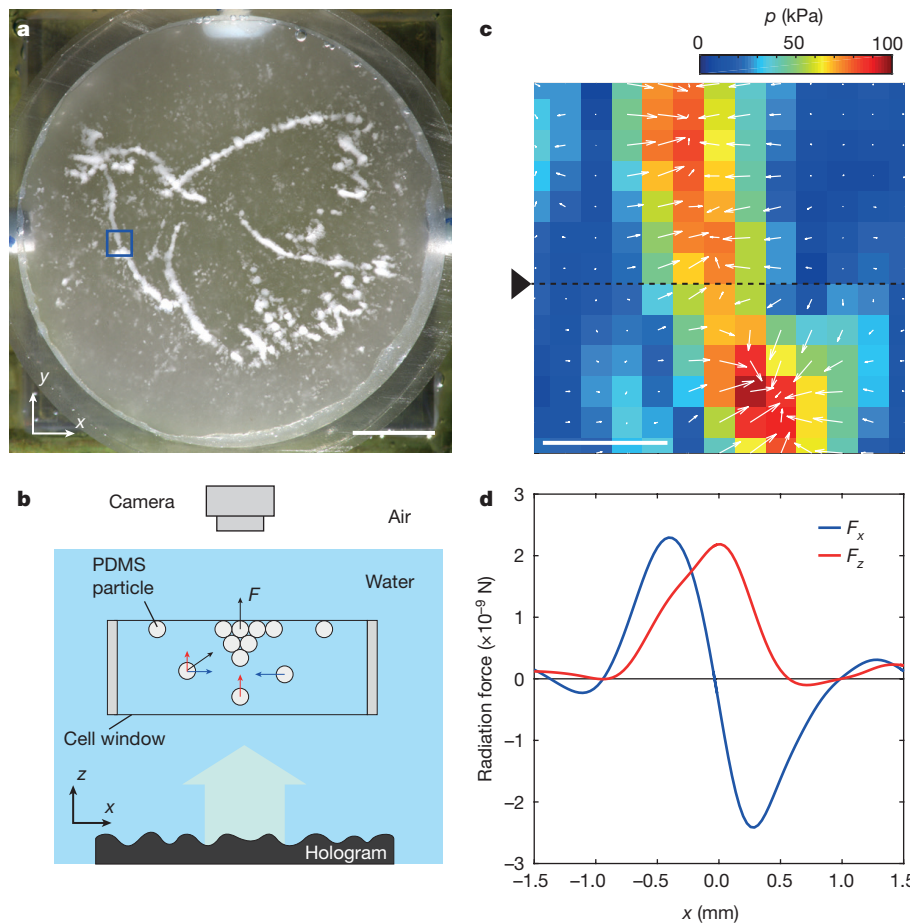


Figure 2 | Assembling particles into asymmetric 2D shapes.

a, Photograph of PDMS microspheres assembled by the acoustic intensity gradient of the particle trap in operation. Blue square marks area of **c**. Scale bar, 10 mm. **b**, Schematic of the experimental set-up and assembly mechanism: the particles are pushed into the transparent barrier by F_z and gathered in-plane by the lateral acoustic gradient forces F_x and F_y . **c**, Detail of the experimentally measured and scaled acoustic pressure

(p) distribution and resulting force vectors for 150- μm -diameter PDMS particles. The dashed line indicates the position of the force component profiles plotted in **d**. Scale bar, 1 mm. **d**, Plot of acoustic radiation forces F_x , F_z along the dashed cut line in **c** calculated from the angular spectrum decomposition (see Methods). More details are shown in Extended Data Figs 6 and 7. The trap in operation is shown in Supplementary Video 1.

non-destructive testing and medical diagnostic ultrasound⁸, which in water has a wavelength of $\lambda \approx 750 \mu\text{m}$. Printing with a modest $375\text{-}\mu\text{m}$ resolution ($\sim\lambda/2$) we achieve 15,000 acoustic pixels in the hologram, which is already one order of magnitude higher than what has been achieved with PATs^{8,9}. Furthermore, computation and fabrication of the hologram is straightforward (see Methods), and the system scales to large apertures and smaller pixel sizes without adding complexity. The especially fine print resolution ($20 \mu\text{m}$) in the sound propagation direction (z direction) allows us to encode 100 phase steps over the full range of 2π rad of the passing wave. This improves the signal to noise ratio of the image by eliminating unwanted phase discretization effects to improve the diffraction efficiency. Furthermore, the principle of holographic redundancy means that it is possible to encode multiple image planes with distinct intensity distributions in a single hologram (see Extended Data Figs 3 and 4)¹⁷. Although this comes at the expense of quality (or homogeneity), because the hologram must now store multiple images within the same fixed information content, the exceptionally large SW of our holograms makes it possible to maintain high reconstruction fidelity. This technique allows for 3D sculpting of the transmitted acoustic field.

The manipulation of objects by sound fields is one discipline that stands to benefit from greater control over the 3D amplitude and phase distribution in the working volume^{3,18}. Current acoustic manipulation techniques can be broadly divided between assembly schemes, which collect an ensemble of many particles into one or more extended regions^{18,19}, and tweezer-based approaches, where a small number of localized point minima each trap a particle^{3,11,20}. Because assembly schemes rely on resonator structures with standing-wave pressure fields that are highly symmetric, the resulting assemblies are themselves symmetric²¹. On the other hand, tweezer methods must actively change the trap geometry to reposition particles once they are captured, either by moving the transducer²², or by adjusting the phase of a PAT^{3,23}. With acoustic holograms we achieve both extended potentials capable of assembling ensembles of particles into arbitrary static shapes, and dynamic, tweezer-like traps that simultaneously confine and propel objects.

We demonstrate asymmetric particle assembly by introducing a suspension of polydimethylsiloxane (PDMS) microparticles (see Methods) into the workspace beyond the holographic element (Fig. 2). The particles are contained in a cell bounded by thin acoustically transparent windows, which allow the acoustic wave to pass through the container with little reflection and maintain its travelling-wave character. When the ultrasound transducer is turned on, the acoustic radiation force pushes the particles up (away from the hologram) until they are constrained by the top window, which is arranged to be coplanar with the reconstruction image plane (Fig. 2b). The PDMS particles, which have low bulk modulus and a density slightly higher than water, are characterized by a negative acoustic contrast factor and high acoustic attenuation²⁴. Once constrained, this causes the particles to migrate transversely with the pressure gradient towards areas of high sound pressure. The forces shown in Fig. 2c, d are calculated²⁵ from the sound pressure map measured in the image plane (see Methods). The dynamics of the full trap in operation can be seen in Fig. 2a and Supplementary Video 1. Thus we can use particle trapping to produce a high-fidelity, high-resolution replica of a chosen amplitude image in a material medium. When the sound is turned off the particles disperse, falling under the influence of gravity.

Holograms are capable of reconstructing not only arbitrary intensity images but also, simultaneously, any desired phase profile. Of particular importance for object manipulation are uniform phase gradients. These have been used with optical tweezers to induce particle movement in elongated traps²⁶. Similarly, helical acoustic waves have been used to transfer angular momentum to levitated objects in highly symmetric geometries based on the same principle^{10,12}. The driving force arises because a phase gradient in an observation plane is simply the

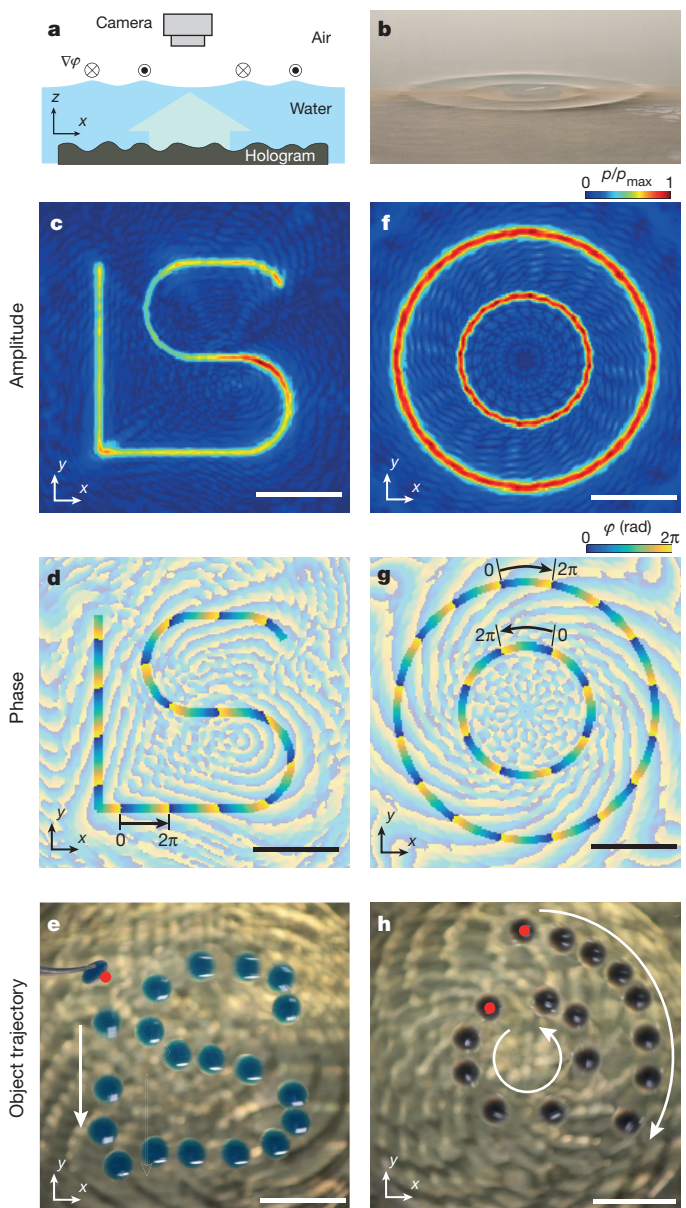


Figure 3 | Phase-gradient surfers. High-information-content holograms permit independent control of the amplitude (c, f) and phase (d, g) distributions in the image plane. **a**, Experimental set-up showing the hologram and the crests formed at the water–air interface by the acoustic field and the direction of the phase gradient ($\nabla\varphi$) on the crests. **b**, Oblique angle photograph of the crests formed by the hologram in f–h. **c, d**, Virtual reconstructions of the projected amplitude (c) and phase (d) image of an open track. The areas of high pressure in the amplitude target image have been highlighted in the phase map. **e**, Experimental time-lapse sequence of a single object placed at the start of the crest (red dot) defined by the intensity maximum following the phase gradient along the track. **f, g**, Calculated amplitude (f) and phase (g) images of two closed concentric tracks having phase gradients of opposite signs. **h**, Time-lapse sequence of two objects placed on the rings and moving in counter-propagating directions. The objects orbit as long as the sound field is active. See Supplementary Videos 2 and 3 for recordings of particle motion and a virtual z-scan of amplitude and phase for the open track, respectively. All scale bars, 10 mm.

in-plane component of the beam propagation direction, and thus the corresponding component of the radiation force. Unlike the pressure gradient force, whose sign depends on the material composition of the particle in relation to the surrounding medium (that is, the acoustic contrast factor), the direction of the force resulting from a phase gradient is the same for all particles²⁷.

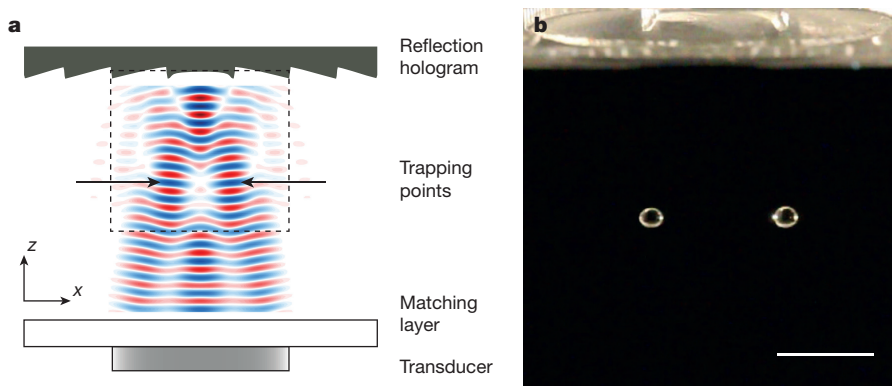


Figure 4 | Reflection hologram for acoustic levitation in air. **a**, Side-view schematic of the cavity set-up, showing the 100 kHz transducer beneath the reflection hologram and the Gor'kov potential of the resulting standing wave. The two trapping points (arrows) are separated by 2λ . **b**, Two water

We designed holograms that project an amplitude image of a curvilinear track of constant high pressure with a superimposed uniform phase gradient of $\sim 1 \text{ rad mm}^{-1}$. With the transducer and hologram positioned to generate a focus at the water surface, the tracks defined by the high-pressure regions are clearly visible as static crests on the water surface (Fig. 3a, b). Objects that are positioned on a crest are trapped in a local minimum of capillary energy and are therefore constrained to move along the track. The projected pressure image defines the path that the particle can take and the phase gradient provides the driving force to push the particle along it. Figure 3c, f shows computed reconstructions (top views) of the amplitude of two complex trajectories that constrain the objects. The corresponding phase profiles are shown in Fig. 3d, g. An object that is manually placed at the start (red dot) of the open track (Fig. 3e) acts as phase-gradient surfer and will follow the whole path until the end (and then float away). Figure 3f–h shows two concentric circular paths with opposite angular phase gradients. Particles placed on these rings will follow the paths indefinitely, until the ultrasound transducer is turned off. These periodic orbits are dependent on the cyclic nature of phase, and would be impossible in any system driven by static gradients in acoustic pressure. Note too that, relative to established acoustic tweezers techniques, this approach offers a simpler method to move particles because it requires no defined starting location (an object placed at any point along the track will follow the trajectory), and no real-time computation and modification of the acoustic field.

Finally, the same principles behind acoustic transmission holograms can also be used to generate reflection holograms. We apply this to a different domain, ultrasound in air, and shape the 3D acoustic field within a cavity geometry, as shown in Fig. 4a. Because the wavelength of sound in air ($\lambda = 3.4 \text{ mm}$) is longer than in water, the information content of the image is strongly diffraction limited and we are restricted to comparatively simple images (more details are available in Methods). Nevertheless, Fig. 4 shows a cavity with a hologram reflector that generates two transverse traps, offset by 3 mm ($\sim \lambda$) from the cavity axis, each capable of levitating water droplets and solid objects with densities up to that of aluminium ($\rho = 2.7 \text{ g cm}^{-3}$) (see also Extended Data Fig. 5 and Supplementary Video 4). Conventional cavities^{20,28} support trapping by standing waves only at the cavity's symmetry axis. We expect that with larger, more powerful transducers it will be possible to generate images with more complexity, and to manipulate objects with higher densities.

In summary, we have introduced the acoustic hologram. Its 3D-printed surface profile encodes the phase of the desired wavefront. The reported system can shape sound fields with significantly higher degrees of freedom than conventional phased array transducers, at a fraction of the cost and complexity. These holograms are particularly well suited to the short wavelengths of high-frequency ultrasound in water: modern 3D printers can readily achieve 100- μm

droplets levitated in the traps. Their transverse positions, away from the centre-line of the cavity, are defined by the hologram. Field of view corresponds to dashed rectangle in a. Scale bar, 5 mm. See Supplementary Video 4 and Extended Data Fig. 5.

lateral resolution^{29,30}, permitting diffraction-limited pixels at 7.5 MHz. Such a hologram with a 50 mm aperture would contain 192,000 pixels. This makes acoustic holograms suitable for operation throughout the frequency range used in most ultrasound applications. But as we have shown, the holograms can also be used as reflection elements in air to levitate dense solids and liquids within complex traps. Although these holograms offer the benefits of high information content, preprogrammed function, and simplicity of reconstruction, they suffer the disadvantage that they cannot be dynamically reconfigured like classic tweezers. Nevertheless, dynamic behaviour can be achieved using the demonstrated phase propulsion techniques. Alternatively, multiple images can be encoded for reconstruction by distinct frequencies; the image to be projected can then be selected, dynamically, by the excitation frequency. Since separating the tasks of generating the sound field and encoding the phase information simplifies the fabrication of the components responsible for each, this approach is particularly attractive for high-power ultrasound devices.

The manipulation experiments that we have presented can be applied to other applications in contactless material handling. However, the dominant applications for ultrasound remain non-destructive evaluation, and diagnostic and therapeutic medical ultrasound. It is here that we expect the acoustic hologram to have the greatest impact, as it permits rapid fabrication of complex sound fields appropriate for super-resolution imaging, selective heating, and personalized medicine.

Online Content Methods, along with any additional Extended Data display items and Source Data, are available in the online version of the paper; references unique to these sections appear only in the online paper.

Received 23 March; accepted 12 August 2016.

1. Tay, S. *et al.* An updatable holographic three-dimensional display. *Nature* **451**, 694–698 (2008).
2. Grier, D. G. A revolution in optical manipulation. *Nature* **424**, 810–816 (2003).
3. Marzo, A. *et al.* Holographic acoustic elements for manipulation of levitated objects. *Nat. Commun.* **6**, 8661 (2015).
4. Hertzberg, Y. & Navon, G. Bypassing absorbing objects in focused ultrasound using computer generated holographic technique. *Med. Phys.* **38**, 6407–6415 (2011).
5. Gabor, D. A new microscopic principle. *Nature* **161**, 777–778 (1948).
6. Leith, E. N. & Upatnieks, J. Reconstructed wavefronts and communication theory. *J. Opt. Soc. Am.* **52**, 1123–1130 (1962).
7. Dallas, W. J. in *Digital Holography and Three-Dimensional Display* Ch. 1 (ed. Poon, T.) 1–49 (Springer, 2006).
8. Szabo, T. L. *Diagnostic Ultrasound Imaging: Inside Out* 2nd edn (Academic, 2014).
9. Drinkwater, B. W. & Wilcox, P. D. Ultrasonic arrays for non-destructive evaluation: a review. *NDT Int.* **39**, 525–541 (2006).
10. Demore, C. E. *et al.* Mechanical evidence of the orbital angular momentum to energy ratio of vortex beams. *Phys. Rev. Lett.* **108**, 194301 (2012).
11. Baresch, D., Thomas, J. L. & Marchiano, R. Observation of a single-beam gradient force acoustical trap for elastic particles: acoustical tweezers. *Phys. Rev. Lett.* **116**, 024301 (2016).
12. Anhäuser, A., Wunenburger, R. & Brasselet, E. Acoustic rotational manipulation using orbital angular momentum transfer. *Phys. Rev. Lett.* **109**, 034301 (2012).

13. Goodman, J. W. *Introduction to Fourier Optics* 3rd edn (Roberts & Co., 2005).
14. Xu, L., Peng, X., Guo, Z., Miao, J. & Asundi, A. Imaging analysis of digital holography. *Opt. Express* **13**, 2444–2452 (2005).
15. Lesem, L. B., Hirsch, P. M. & Jordan, J. A. The kinoform: a new wavefront reconstruction device. *IBM J. Res. Dev.* **13**, 150–155 (1969).
16. Mellin, S. & Nordin, G. Limits of scalar diffraction theory and an iterative angular spectrum algorithm for finite aperture diffractive optical element design. *Opt. Express* **8**, 705–722 (2001).
17. Haist, T., Schonleber, M. & Tiziani, H. J. Computer-generated holograms from 3D-objects written on twisted-nematic liquid crystal displays. *Opt. Commun.* **140**, 299–308 (1997).
18. Caleap, M. & Drinkwater, B. W. Acoustically trapped colloidal crystals that are reconfigurable in real time. *Proc. Natl Acad. Sci. USA* **111**, 6226–6230 (2014).
19. Courtney, C. R. P. et al. Manipulation of particles in two dimensions using phase controllable ultrasonic standing waves. *Proc. R. Soc. A* <http://dx.doi.org/10.1098/rspa.2011.0269> (2011).
20. Foresti, D., Nabavi, M., Kingauf, M., Ferrari, A. & Poulikakos, D. Acoustophoretic contactless transport and handling of matter in air. *Proc. Natl Acad. Sci. USA* **110**, 12549–12554 (2013).
21. Oberti, S., Neild, A. & Dual, J. Manipulation of micrometer sized particles within a micromachined fluidic device to form 2D patterns using ultrasound. *J. Acoust. Soc. Am.* **121**, 778–785 (2007).
22. Lee, J. et al. Single beam acoustic trapping. *Appl. Phys. Lett.* **95**, 073701 (2009).
23. Courtney, C. R. P. et al. Independent trapping and manipulation of microparticles using dexterous acoustic tweezers. *Appl. Phys. Lett.* **104**, 154103 (2014).
24. Johnson, L. M. et al. Elastomeric microparticles for acoustic mediated bioseparations. *J. Nanobiotechnol.* **11**, 22 (2013).
25. Sapozhnikov, O. A. & Bailey, M. R. Radiation force of an arbitrary acoustic beam on an elastic sphere in a fluid. *J. Acoust. Soc. Am.* **133**, 661–676 (2013).
26. Roichman, Y., Sun, B., Roichman, Y., Amato-Grill, J. & Grier, D. G. Optical forces arising from phase gradients. *Phys. Rev. Lett.* **100**, 013602 (2008).
27. Chen, X. & Apfel, R. E. Radiation force on a spherical object in an axisymmetric wave field and its application to the calibration of high-frequency transducers. *J. Acoust. Soc. Am.* **99**, 713–724 (1996).
28. Xie, W. J. & Wei, B. Parametric study of single-axis acoustic levitation. *Appl. Phys. Lett.* **79**, 881–883 (2001).
29. Tumbleston, J. R. et al. Continuous liquid interface production of 3D objects. *Science* **347**, 1349–1352 (2015).
30. Studart, A. R. Additive manufacturing of biologically-inspired materials. *Chem. Soc. Rev.* **45**, 359–376 (2016).

Supplementary Information is available in the online version of the paper.

Acknowledgements We thank P. Weber and M. Fratz for suggestions. This work was in part supported by the Max Planck Society and by the European Research Council (ERC grant agreement 278213).

Author Contributions P.F. initiated the project. K.M. conceived of the hologram and developed the workflow for the hologram generation. T.Q. fabricated the holograms. K.M. and A.G.M. designed and performed the experimental demonstrations. P.F. directed the research project. A.G.M., K.M. and P.F. wrote the manuscript.

Author Information All photographs were taken by the authors. The target image of the dove in Fig. 1a is a modified rendition of a picture for which the authors hold a commercial license, and is available at <https://www.vectoropenstock.com/vectors/preview/71432/whitedove-laurel-peace-symbol>. The authors declare competing financial interests: details are available in the online version of the paper. Reprints and permissions information is available at www.nature.com/reprints. Readers are welcome to comment on the online version of the paper. Correspondence and requests for materials should be addressed to P.F. (fischer@is.mpg.de).

Reviewer Information *Nature* thanks B. Drinkwater, A. Nield and the other anonymous reviewer(s) for their contribution to the peer review of this work.

METHODS

Information content of holograms and the diffraction limit. The space bandwidth product of the hologram (h) is $SW_h = N \times N = (L/d)^2$, where L and d are the lateral sizes of the hologram and each pixel, respectively, and N is the number of pixels in each dimension. On the other hand, the space bandwidth product of the image (i) is $SW_i = L^2 B^2$ where B is the spatial bandwidth of the image¹³. Free space propagation cannot increase the space bandwidth product, so $SW_i \leq SW_h$. But the upper bound of the image's spatial bandwidth is set by the diffraction limit, $\sim \lambda/2$, so that $B \lesssim 2/\lambda$, and $SW_i \lesssim 4L_x L_y / \lambda^2$. Diffraction-limited performance is achieved when $SW_h = SW_i$, which reduces to $d = \lambda/2$.

Wave propagation. Because the hologram information is stored mostly in its phase profile (transmission losses $\alpha_T(x,y)$ are low) it is critical to use the exact phase term for propagating the wave during iteration. We use the angular spectrum method³¹, as it performs well, yields the exact phase and has low computational cost. The acoustic pressure wave is expressed as

$$p(x, y, z) = \hat{p}(x, y, z) e^{j\Delta\phi(x, y, z)} \quad (1)$$

where the explicit time dependence has been dropped, and where $\hat{p}(x, y, z)$ and $\Delta\phi(x, y, z)$ are the amplitude and phase function maps, respectively. The angular spectrum of this wave in a plane at constant z is obtained by the Fourier transform:

$$P(k_x, k_y, z) = \iint_{-\infty}^{+\infty} p(x, y, z) e^{-j(k_x x + k_y y)} dx dy \quad (2)$$

We define $z=0$ to be the hologram plane. Once $P(k_x, k_y, 0)$ is known, the angular spectrum at any plane downstream can be calculated by multiplying the angular spectrum with a propagator function

$$P(k_x, k_y, z) = P(k_x, k_y, 0) H(k_x, k_y, z) \quad (3)$$

$$H(k_x, k_y, z) = e^{jz\sqrt{k^2 - k_x^2 - k_y^2}}$$

where $k_m = |\mathbf{k}| = \omega/c$ is the wavenumber in the liquid medium, ω the angular frequency, c the speed of sound in the medium, and the wave vector $\mathbf{k} = (k_x, k_y, k_z)$. The real-space pressure field in any plane z can be obtained via the inverse Fourier transform:

$$p(x, y, z) = \frac{1}{4\pi^2} \iint_{-\infty}^{+\infty} P(k_x, k_y, z) dk_x dk_y \quad (4)$$

Backpropagation from the image to the hologram can be calculated with

$$P(k_x, k_y, 0) = P(k_x, k_y, z) H(k_x, k_y, -z) \quad (5)$$

The limited size of the observation window leads to a cut-off of higher spatial frequencies over the propagation distance. We therefore limit the integration region of the inverse Fourier transform to account for the cut-offs³². A simple geometrical estimate yields

$$k_{x,y} \leq \frac{\pi(L_h + L_i)}{\lambda \sqrt{\frac{1}{4}(L_h + L_i)^2 + \Delta z^2}} \quad (6)$$

where λ is the wavelength in the medium, and L_h, L_i are the side lengths of the observation windows in the hologram and image planes, respectively. The computational domain is limited in space, which has the effect that over large propagation distances higher spatial frequencies will be reflected at the domain boundaries (aliasing). Subsequent back-propagation and multiple iterations (as required by the IASA) will push these erroneous components towards the area of interest. We therefore extend the computational domain to allow all bandwidth-limited spectral components emanating from the hologram or image aperture to propagate without aliasing. This leads to a domain size of $L_d \geq 3 \times \max\{L_h, L_i\}$. The field outside the hologram aperture is then set to zero.

Computation of acoustic holograms. To compute the hologram we use the iterative angular spectrum approach (IASA)¹⁶. The underlying angular spectrum method keeps the exact phase term for the propagation and performs well in the nearfield at low computational cost^{31,32}. The phase distribution of a hologram is computed by propagating a wave from the image plane to the hologram plane and back, which is then repeated and iteratively optimized. In each iteration we adjust the complex values of the field in the hologram plane and the image plane to the desired constraints. After a few tens of iteration cycles the algorithm converges to a phase map in the plane of the holographic element. The IASA can be extended to

encode multiple images in one hologram. Since the radiation force on a spherical particle in an arbitrary acoustic travelling wave can be calculated from its angular spectrum²⁵, these calculations also serve as a basis for estimating radiation forces.

We start by defining the constraints for each plane of interest. In the hologram plane the amplitude is set to the transducer output pressure distribution, $\hat{p}_0(x, y)$, which we have measured close to the transducer and numerically back-propagated to the transducer face. We assume a flat phase output of the transducer and set the hologram phase initially to zero. The constraints (boundary conditions) for each image plane are set separately. For the example provided in Extended Data Fig. 8, the boundary conditions are the pressure distribution for each image with no constraints on the phase. If instead a phase gradient is sought, as in Fig. 3, the boundary condition is the phase distribution and is defined as a second map located in the same plane, with no constraints on the amplitude.

The following steps are repeated until a satisfying image quality is obtained (in step 2). Typically, 20 to 50 iterations are required for the holograms of this paper. See Extended Data Fig. 8 for a schematic illustration. The steps for producing amplitude (phase) images are those of ref. 16 with extensions to multiple image planes and phase constraints:

- (1) Propagate the field from the hologram to each image plane.
- (2) Evaluate the quality of the projected image for each image plane.
- (3) Reset the amplitude (phase) for each image plane to match the target value. The forward-propagated phase (amplitude) is retained.
- (4) Separately propagate the field for each image plane back to the hologram.
- (5) Sum all back-propagated complex fields in the hologram plane.
- (6) Compute the thickness of the hologram pixels using equation (8), and the transmission coefficient $\alpha_T(x, y)$ using equation (7).
- (7) Set the complex amplitude at the hologram plane to $\hat{p}(x, y, 0) = \sqrt{\alpha_T} \hat{p}_0(x, y)$.
- (8) Repeat from step 1.

For simplicity we assume that the hologram is a thin element and therefore treat each pixel as a one-dimensional transmission line. The transmission coefficient

$$\alpha_T(x, y) = \frac{4Z_t Z_h^2 Z_m}{Z_h^2 (Z_t + Z_m)^2 \cos(k_h T(x, y))^2 + (Z_h^2 + Z_t Z_m)^2 \sin(k_h T(x, y))^2} \quad (7)$$

relates the input power to the output power for each pixel. $Z_i = \rho_i c_i$ is the acoustic impedance, ρ_i the density, c_i the speed of sound of layer i and the subscripts t, h, m denote materials for the transducer face, hologram and medium, respectively. The acoustic properties of the cell used to contain the particles in Fig. 2a are not included in the calculation.

Using the final phase map and equation (8) we compute the final thickness map $T(x, y)$. This matrix is then converted to a mesh in the Standard Tessellation Language (STL) format, which serves as input to the 3D printer.

Fabrication of acoustic holograms. The IASA output provides a phase map for the holographic element, which we then translate to a surface map for fabrication. The hologram plate begins with an initial thickness T_0 . Removing material at pixel position (x, y) leads to a relative phase change

$$\Delta\phi(x, y) = (k_m - k_h) \Delta T(x, y) \quad (8)$$

where $T(x, y) = T_0 - \Delta T(x, y)$ is the thickness of the pixel positioned at coordinates (x, y) in the hologram plane and k_h, k_m are the wave numbers in the hologram body and its surrounding medium, respectively. The resulting thickness map is then printed with a 3D printer (Objet Connex 260, Stratasys) in VeroClear material. At 2 MHz we measured the speed of sound and the sound attenuation in this material to be 2,424 m s⁻¹ and 5.5 dB cm⁻¹, respectively. The measurement is based on analysing the time of flight and amplitude of ultrasonic pulses through solid blocks of differing side lengths.

Computation of reflection acoustic holograms. Reflection holograms are computed in a manner similar to what was used for the in-water transmission holograms. In this case, the transducer output is first propagated to the hologram plane opposite to establish the input field across the hologram aperture. Then the hologram solution is found using the same IASA procedure. If the target region lies between transducer and hologram, the transducer output has to be separately propagated to the target plane and added to the reflected field in each iteration. We use only three waves in our cavity calculation: the initial transducer output, the hologram reflection, and that reflected in turn from the transducer face. Thus we are assuming an inefficient cavity with very low quality factor. The strong acoustic mismatch between air and the polymer hologram means that the first reflection is very efficient. The phase and thickness for a reflection hologram are related as

$$\Delta\phi(x, y) = 2k_m \Delta T(x, y). \quad (9)$$

Print quality. To assess the 3D-print quality of the hologram, X-ray computed tomography (CT) was performed using a TomoScope HV 500 (Werth GmbH,

Germany) with a voxel size of $81\text{ }\mu\text{m} \times 81\text{ }\mu\text{m} \times 81\text{ }\mu\text{m}$. The results are shown in Extended Data Fig. 1. Extended Data Fig. 1a–c shows the designed thickness map before printing, the measured thickness map from the CT analysis, and the difference of the two, respectively. Extended Data Fig. 1d–f shows plots of the designed and measured surface profile along different horizontal slices through the sample. The desired thickness map and the achieved 3D-printed hologram are in excellent agreement, although the printing process behaves like a low-pass filter, smoothing out sharp edges and fine features. For comparison with dimensions along the x -axis, the wavelength λ is indicated in Extended Data Fig. 1d.

Importantly, the CT scan shows a homogeneous density throughout the hologram except at two regions that are marked by red circles in Extended Data Fig. 1b. This is probably due to incomplete curing of the print material in the crevices near the object edges.

Force calculation from measured travelling wave pressure fields. We calculate the radiation force acting on an elastic sphere subjected to a travelling plane wave using the method developed in ref. 27, with some corrections that we made and have documented in the next section. Extended Data Fig. 6a shows the radiation force acting on a spherical particle of polydimethylsiloxane (PDMS) as a function of the particle radius for a 2 MHz incident plane wave with a 100 kPa amplitude. There are sharp resonances at discrete sizes and the general trend is for larger particles to feel stronger forces, but particles of all diameters experience a force of the same sign.

To calculate the force experienced by particles that are subjected to a more complicated sound field, we follow the work of Sapozhnikov *et al.*²⁵ and calculate the radiation force directly from the angular spectrum of the measured field. The angular spectrum decomposes the field into elementary plane waves propagating in different directions. We already know the scattering field for an elementary plane wave. The total scattered field resulting from the arbitrary incident field is the sum of all elementary solutions and the radiation force can then be found by integration.

We start by measuring the acoustic pressure amplitude in the trapping plane. To minimize heating effects over the long (5 h) hydrophone scan, we make the measurement with the transducer driven at low power. We checked for linearity of the transducer and scaled the measured pressure field by a factor of 2.5 to match the higher power conditions used in the trapping experiment. The scaled pressure field is shown in Extended Data Fig. 6b and used as input for the following calculations. Using equation (2), we then calculate the angular spectrum of the field, and the resulting forces using the method in ref. 25. The radiation force is always calculated for a scatterer located at the origin. Therefore, to compute the forces over an area, we need to shift the angular spectrum accordingly. Example force maps are shown for different detailed sections in Extended Data Figs 6c and 7a,b along with the corresponding detail views of assembled particles during the operation of the trap. Extended Data Fig. 6e shows the trapping forces along a specific slice for particles of different sizes.

Corrections to ref. 27. In preparing this work we found two typographical errors in ref. 27 and therefore reprint corrected versions of that work's equations (5) and (6) here. For ease of comparison, we keep the original notation: please refer to ref. 27 for definitions. In equation (6) of ref. 27, the leading minus sign in β_m should be removed such that the parameters are:

$$\alpha_m = -[|D_m|^2 + \text{Im}(D_m)]/[1 + |D_m|^2 + 2\text{Im}(D_m)] \quad (10)$$

$$\beta_m = \text{Re}(D_m)/[1 + |D_m|^2 + 2\text{Im}(D_m)]$$

In addition, the factor 2 in the first term of the denominator of the compound fraction in Φ_m in equation (5) of ref. 27 should be removed, to yield:

$$\Phi_m = \frac{\rho_0(k_s a)^2}{2\rho^*} \frac{1}{m^2 + m - 2 - (k_s a)^2/2} \times \frac{\frac{(m^2 + m)j_m(k_s a)}{j_m(k_s a) + \Lambda_m(k_s a)} + \frac{k_c a j'_m(k_c a)}{\Lambda_m(k_c a)}}{\frac{(m^2 + m)\Lambda_m(k_s a)}{j_m(k_s a) + \Lambda_m(k_s a)} - \frac{j_m(k_c a) + 2\Lambda_m(k_c a)}{\Lambda_m(k_c a)}}. \quad (11)$$

In their corrected form, both equations reproduce the results of the same work and other texts, as well as our experimental results.

Experimental set-up for water. The experimental set-up consists of an open-topped glass tank ($300\text{ mm} \times 300\text{ mm} \times 600\text{ mm}$) that is partially lined with

acoustic absorber sheets (Aptflex F48, Precision Acoustics Ltd, UK) and filled with deionized water (see Extended Data Fig. 9). The piezo transducer is a disk of PZT-5A with a diameter of 50 mm and a thickness of 1 mm, which is fixed to a thin brass plate and mounted in a watertight case so that the back side of the transducer is open to air. A thin layer of vacuum grease (Dow Corning) between the brass plate and the hologram provides good acoustic coupling and temporary mechanical fixing.

A function generator (33120A, Hewlett-Packard) provides the reference signal and a low impedance amplifier directly drives the piezo element via coaxial cables. The operating frequency is 2.06 MHz, near the first thickness resonance of the piezo element.

We used two techniques to measure the sound pressure in the working space. Quantitative, phase sensitive measurements were made using a calibrated needle hydrophone (545 mV MPa^{-1} , 0.5 mm tip diameter, Precision Acoustics Ltd, UK) mounted on a 3D scanning gantry (GAMPT mbH, Germany). The hydrophone amplifier is connected to a lock-in amplifier (UHFLI, Zurich Instruments, Switzerland) referenced to the function generator. A script controls all the instruments and directs scans of the acoustic field in 2D and 3D. The second, qualitative measurement technique used thermochromic films. These undergo a local phase change due to acoustic heating, which results in a visible colour change. The qualitative pressure images acquired with this technique can be seen in Extended Data Fig. 3.

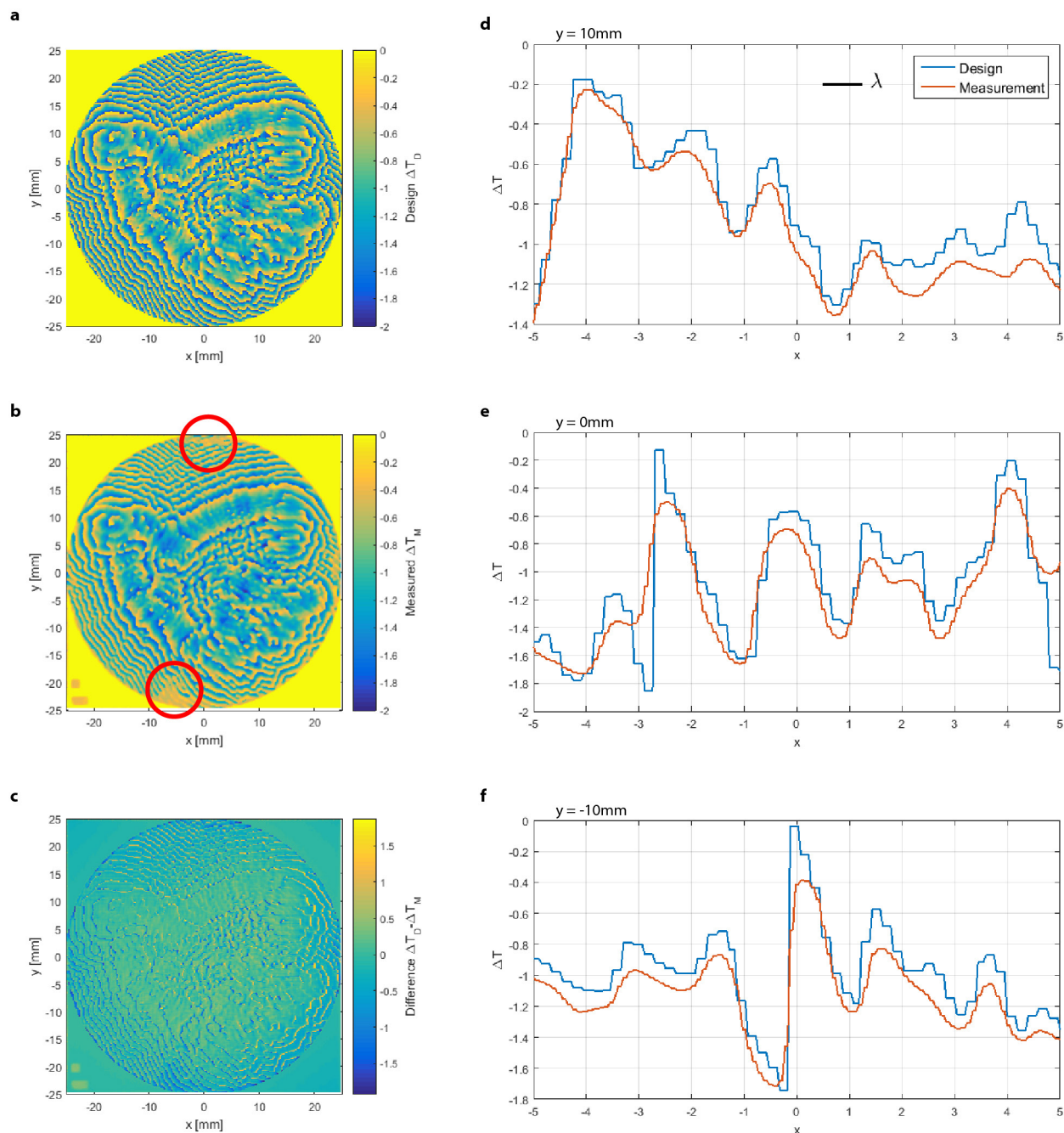
For the particle trapping experiment a cuvette is immersed inside the tank. It is made from a 60 mm diameter acrylic tube, which is cut to 20 mm length. Both ends are covered by a $100\text{ }\mu\text{m}$ thin acoustic window made from polyethylene. The power transmission coefficient is estimated to be 90% for each window using the common 1D transmission line model for a normal incident wave.

Experimental set-up for air. For the levitation experiments in air, the same electronics package described above was used to drive a Multicomp MCUSD40 transducer at 100 kHz. The transducer housing's external diameter is 40 mm, but the piezo's diameter is only 20 mm. The transducer was placed opposite a reflection hologram with an air gap of 25.7 mm between them. The hologram diameter was 40 mm. Experiments were conducted with the cavity oriented vertically (the transducer at either the top or bottom) or horizontally. Trapping lifetimes were around 30 s, limited by the thermal stability and resonance drift of the transducer.

Manipulated particles and objects. We fabricated microparticles of polydimethylsiloxane (PDMS, Sylgard 184, Dow Corning) according to procedure in ref. 24. PDMS base and curing agent were mixed at a ratio of 10:1 and added to a water bath with 1 w% non-ionic surfactant. The emulsion was continuously agitated using a high-speed emulsifier (Turaxx, IKA) while it cured overnight. A microscope image of the suspension can be seen in Extended Data Fig. 6f. The PDMS particles are polydisperse with sizes up to $400\text{ }\mu\text{m}$ diameter. The particles have a density of $1,045\text{ kg m}^{-3}$, speed of sound of $1,020\text{ m s}^{-1}$ (ref. 33), and bulk modulus of 1.1 GPa. Since they are more compressible than water the PDMS particles are attracted to pressure maxima. The acoustic surfers are elastomeric spherical caps with diameters between 2 and 4 mm and thicknesses ranging from 0.5 to 1 mm.

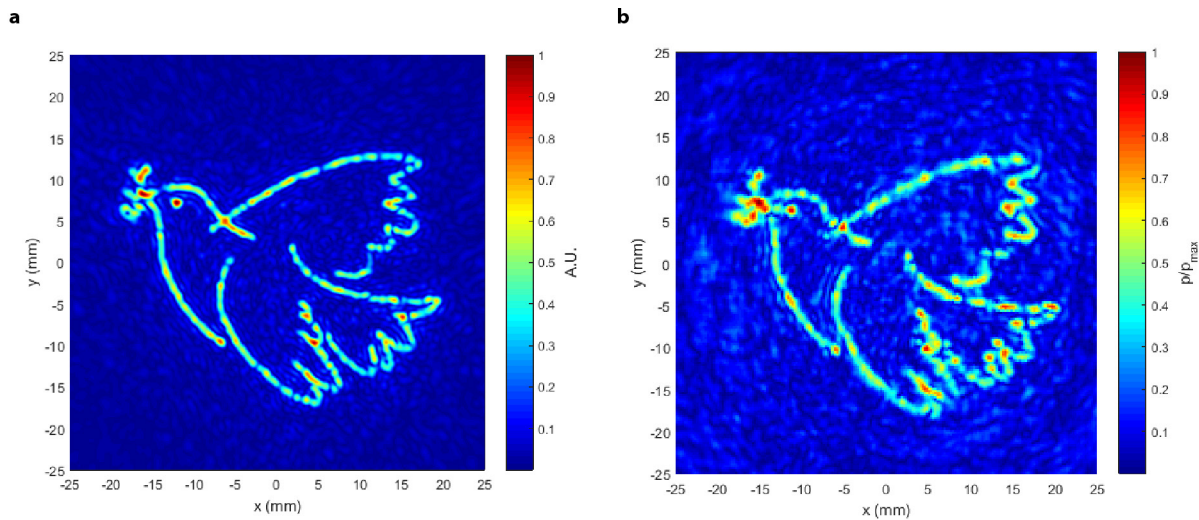
The in-air multi-trap holographic cavity was used to capture particles of glass microballoons ($3\text{ M K20}, <100\text{ }\mu\text{m}, \rho=0.2\text{ g ml}^{-1}$), expanded polystyrene beads (1–3 mm), softwood, lithium metal, polypropylene, silicon, and aluminium ($\rho=2.7\text{ g ml}^{-1}$). The glass microballoons and expanded polystyrene were used as supplied, the other materials were cut into irregular polyhedra with sizes from 0.7 to 2.0 mm. Droplets of isopropyl alcohol and water were also successfully trapped. See Extended Data Fig. 5 for example results. The droplets were loaded by either microsyringe injection directly into selected traps (Fig. 4b), or by aerosolization at the transducer face and coalescence of the resulting mist into multiple traps within the standing wave (Extended Data Fig. 5g–i).

31. Liu, D. L. & Waag, R. C. Propagation and backpropagation for ultrasonic waveform design. *IEEE Trans. Ultrason. Ferroelectr. Freq. Control* **44**, 1–13 (1997).
32. Matsushima, K. & Shimobaba, T. Band-limited angular spectrum method for numerical simulation of free-space propagation in far and near fields. *Opt. Express* **17**, 19662–19673 (2009).
33. Sinha, M. & Buckley, D. J. in *Physical Properties of Polymers Handbook* Ch. 60 (ed. Mark, J. E.) 1021–1031 (Springer, 2007).

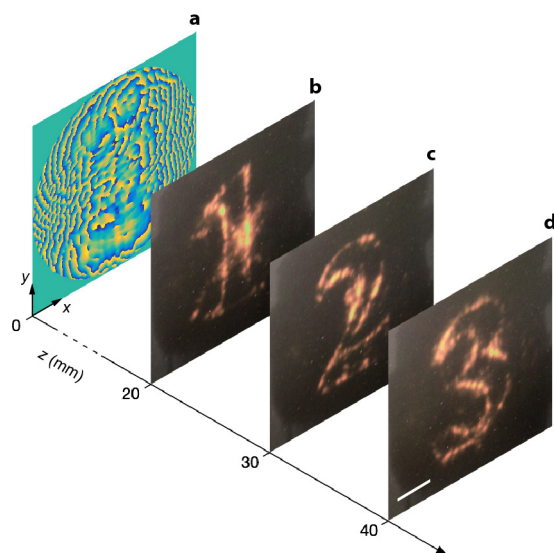


Extended Data Figure 1 | Analysis of the 3D print quality. **a**, Map of design thickness ΔT_D from hologram calculation, as sent to the printer. **b**, Measured thickness ΔT_M map from X-ray computed tomography of the printed hologram. Red circles mark sections of inhomogeneous material

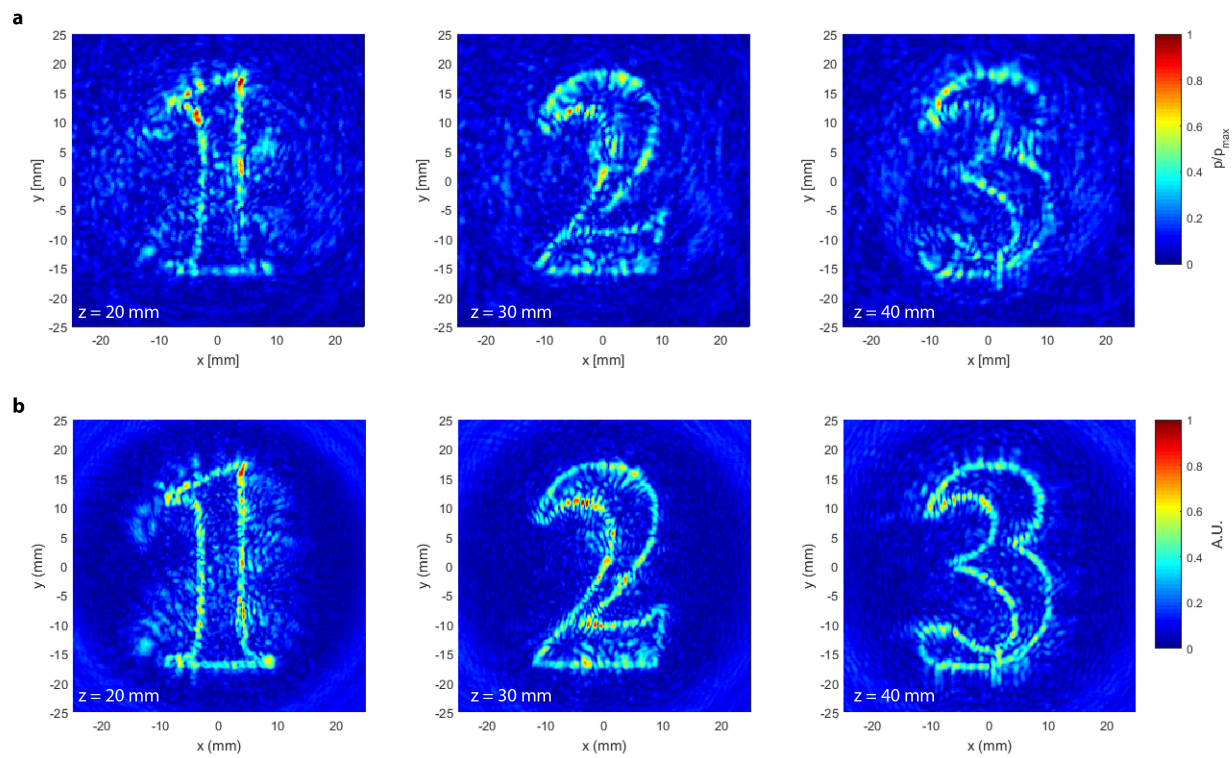
density. **c**, Difference between design (**a**) and measured (**b**) thicknesses. **d–f**, Comparison of thickness profiles ΔT for design (blue) and measurement (red) along $y = 10\text{ mm}$ (**d**), $y = 0\text{ mm}$ (**e**), and $y = -10\text{ mm}$ (**f**). The λ scale bar in **d** shows the wavelength in water at 2.06 MHz.



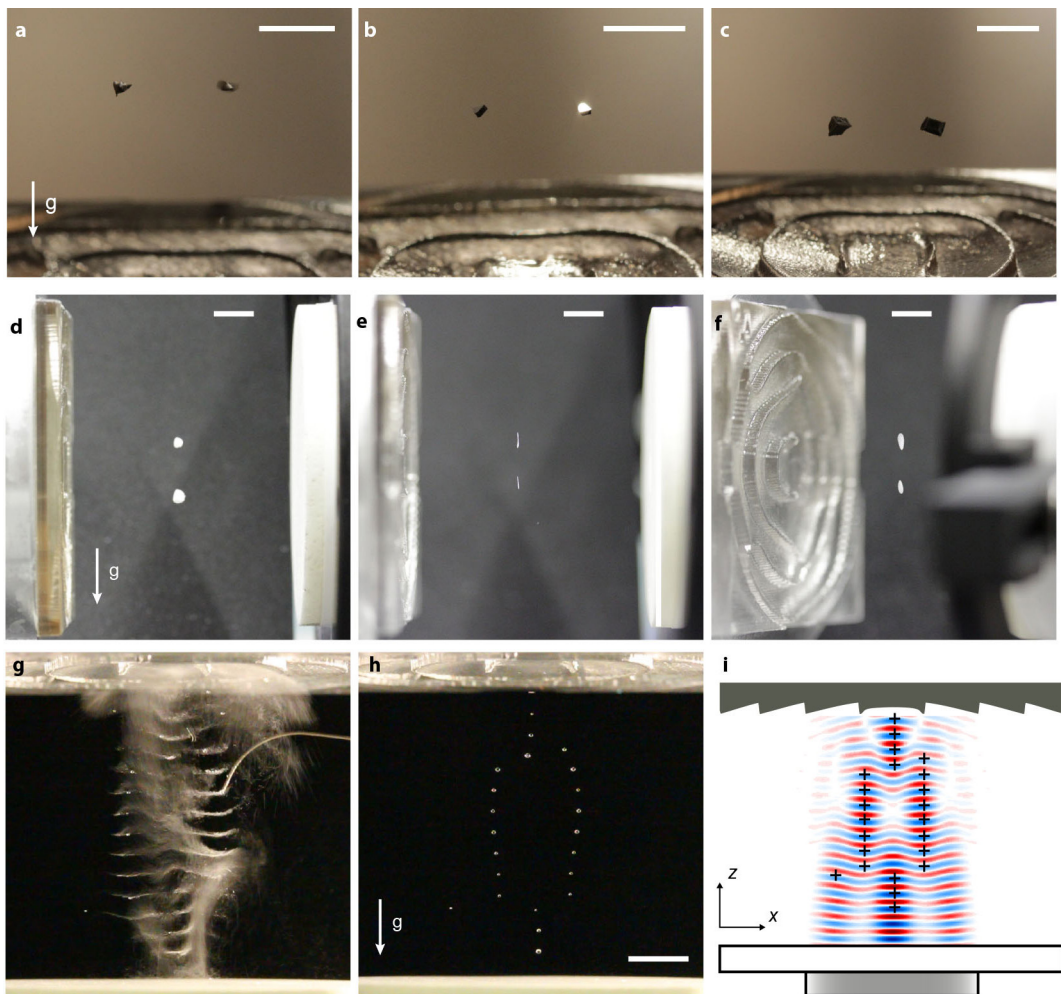
Extended Data Figure 2 | Reconstruction of the target image. **a**, Virtual reconstruction of the pressure field from the final hologram after IASA. **b**, Hydrophone measurement of the acoustic pressure p , normalized by the highest measured pressure p_{\max} , in the plane $z = 30$ mm.



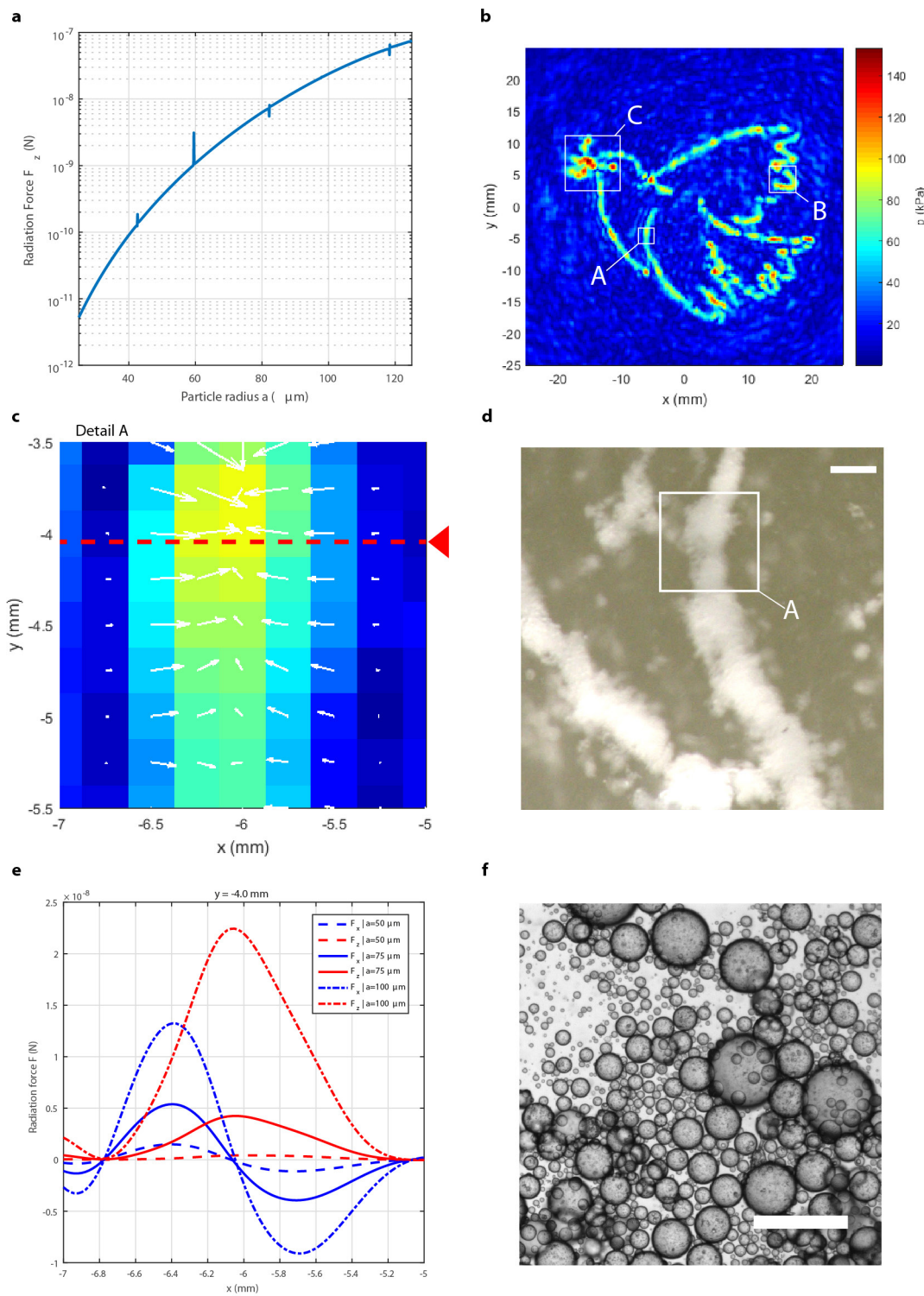
Extended Data Figure 3 | One acoustic hologram can store multiple images in different image planes. Reconstruction yields all images concurrently. **a**, The calculated synthetic phase map recorded in the hologram. **b-d**, Thermochromic detector measurement of local acoustic intensity of the reconstruction at the three independent image planes. Scale bar, 10 mm (applies to all images). See Methods for more details of the measurement, and Extended Data Fig. 4 for complementary hydrophone scans.



Extended Data Figure 4 | Multiple images from one hologram. a, Hydrophone measurements for each image plane. **b,** Virtual reconstruction of the final hologram.

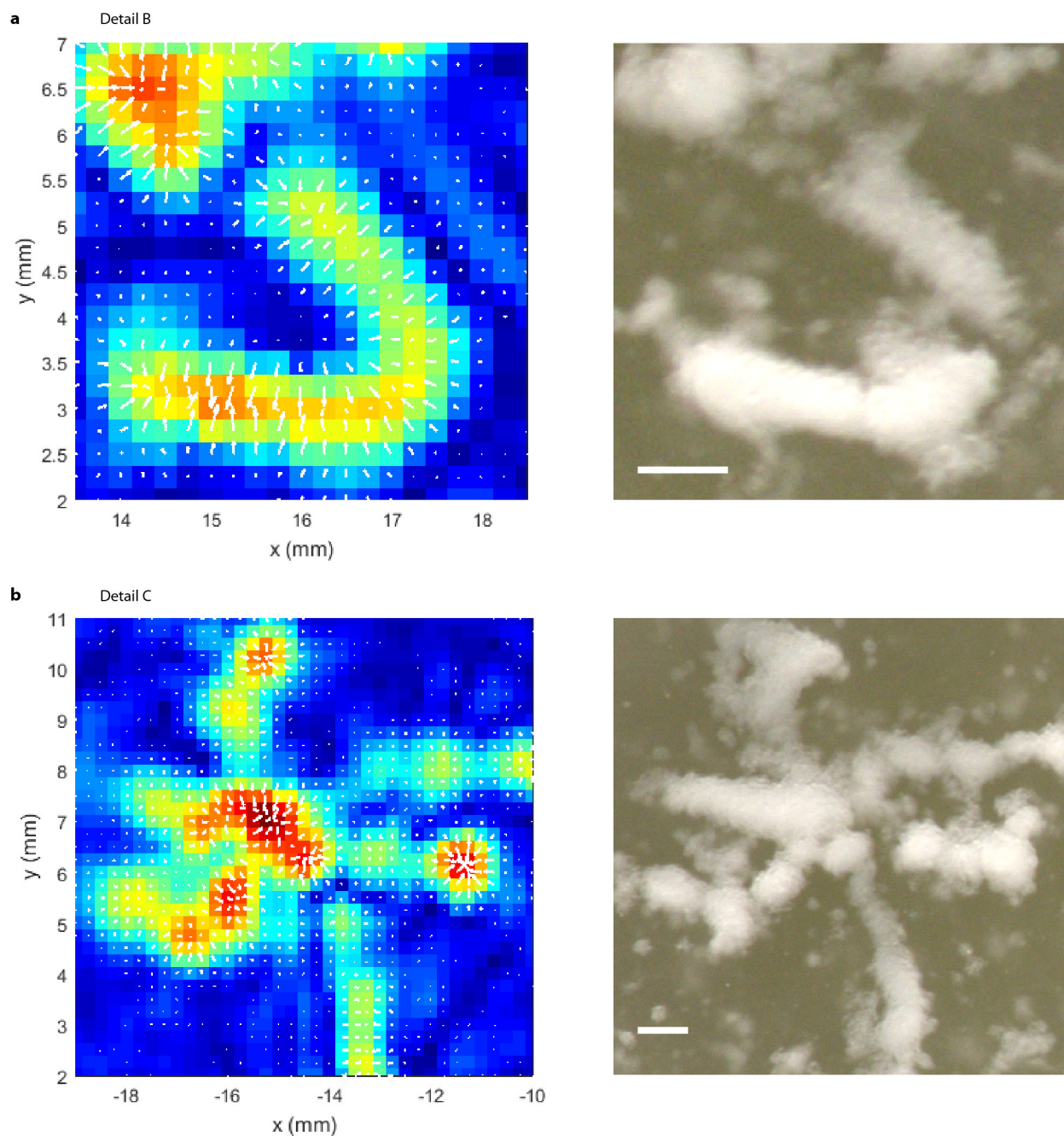


Extended Data Figure 5 | Pictures of levitated objects in air. **a,** Aluminium. **b,** Silicon. **c,** Lithium. **d,** Expanded polystyrene. **e, f,** Hollow glass microspheres. **g,** Water mist, aerosolized at the transducer face. **h,** coalesces into droplets trapped in the acoustic field. **i,** Calculated Gor'kov potential, '+' signs indicate points with trapped droplets in **h.** All scale bars, 5 mm. Gravity is acting downwards in all configurations.

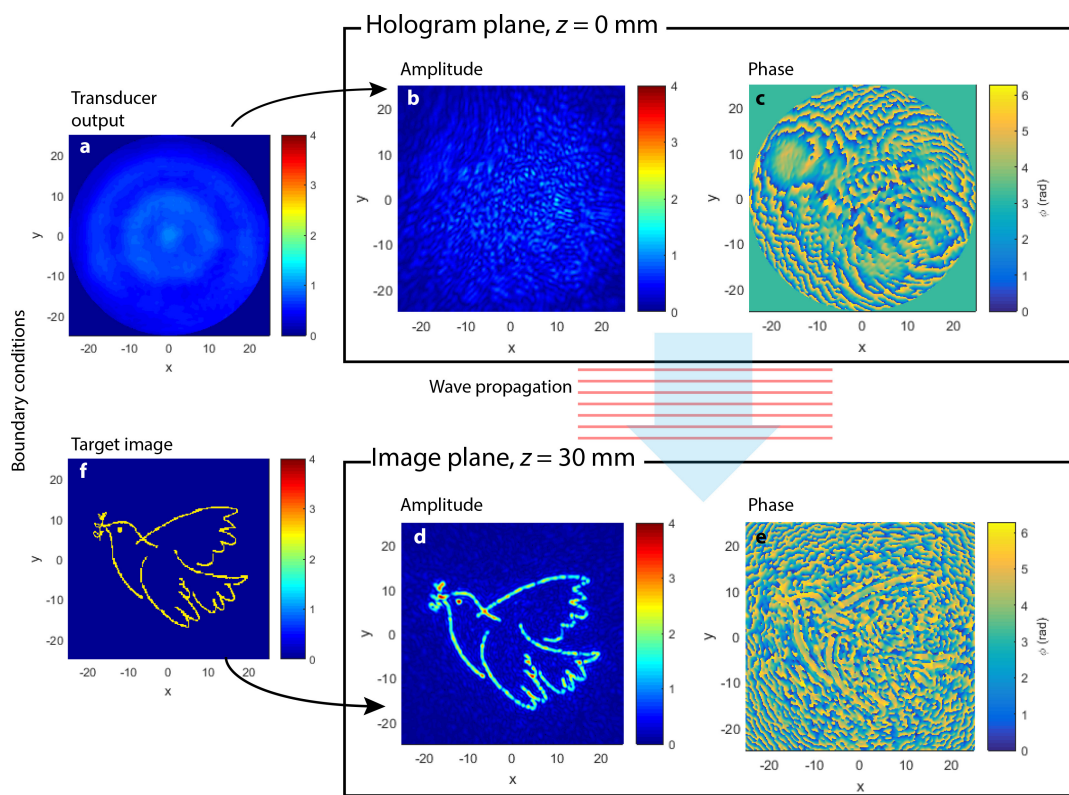


Extended Data Figure 6 | Radiation forces on spherical silicone particles. **a**, Radiation force on a spherical PDMS particle as a function of its radius exposed to a plane travelling wave with frequency $f = 2 \text{ MHz}$, and amplitude $p_0 = 100 \text{ kPa}$. **b**, Low-drive-voltage hydrophone measurement of pressure distribution scaled by factor of 2.5 to match conditions used in the trapping experiments. **c**, Detail of section A with force vectors.

d, Photograph of particles assembled at the pressure maxima in section A. Scale bar, 1 mm. **e**, Forces in x and z direction along the cut line shown in **c** for different particle radii (see key at top right). **f**, Microscopy image of the PDMS particle suspension used in trapping experiments. Scale bar, 300 μm .

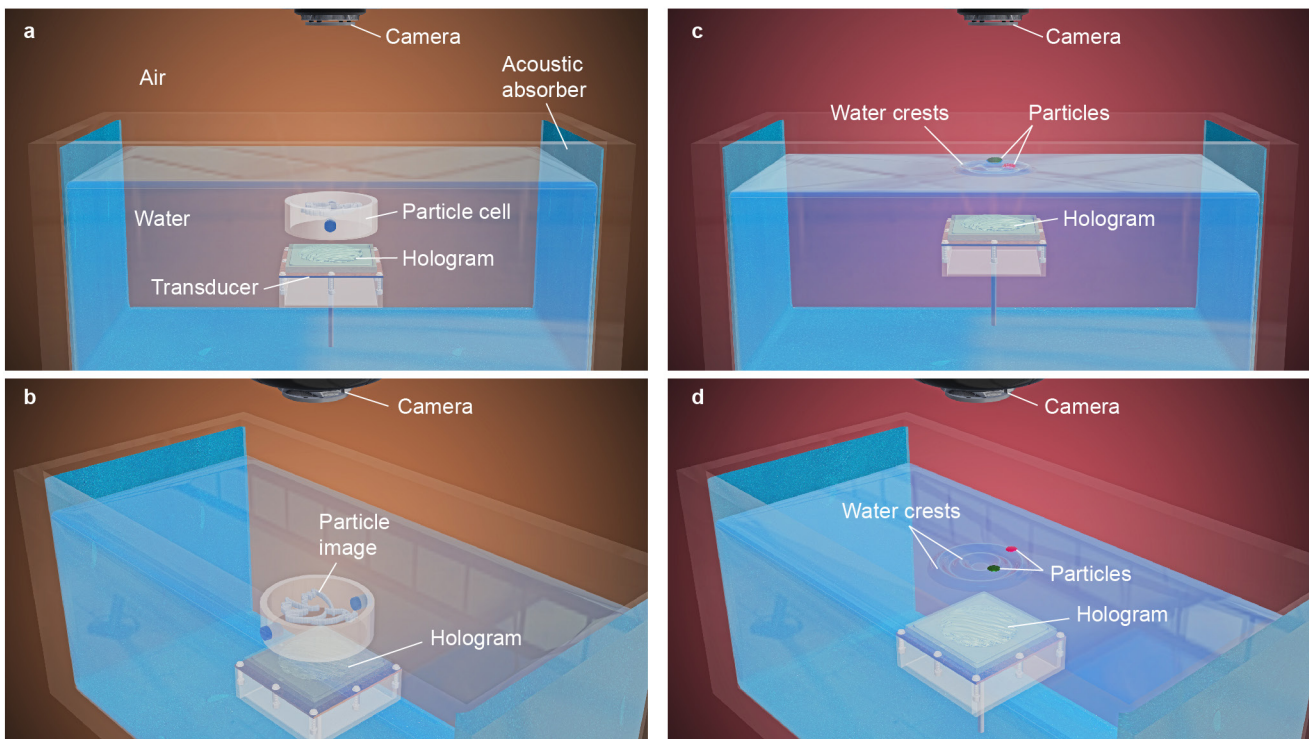


Extended Data Figure 7 | Example sections showing force vectors and corresponding photographs of the particle trap in operation. Panels a and b show results from sections B and C respectively in Extended Data Fig. 6b. Scale bars, 1 mm.


Extended Data Figure 8 | Schematic of the hologram calculation.

a, The transducer output amplitude profile is used as the input boundary condition at the hologram plane. **b, c**, After transmission through the hologram the waveform is propagated (red lines) to **d, e**, the desired image plane, where it is compared with **f**, the target image, in this case a pure amplitude image of the target image. During hologram optimization

the target image amplitude is imposed upon the image plane (the phase is preserved) and then propagated back to the hologram. Again, the amplitude at the hologram plane is set to match that produced by the transducer (accounting for transmission losses) and the process is repeated. After several iterations the optimized reconstructed image (shown here) converges to the target.



Extended Data Figure 9 | Experimental set-up for waterborne ultrasound studies. Experiments were conducted in an open-topped, water-filled glass tank lined on three sides by acoustic absorber. **a**, Side view and **b**, perspective view of the set-up for particle assembly into a target image used to acquire Fig. 2a. The PDMS microparticles are contained within the particle cell located above the hologram. The hologram is mounted on the transducer, which is enclosed in a waterproof box, and projects the soundfield upwards. The cell is arranged so that its upper window coincides with the image plane of the hologram.

Photographs and movies are acquired by the camera mounted above the water's surface. **c**, Side view and **d**, perspective view of the set-up used to demonstrate phase-gradient surfers and acquire Fig. 3. The hologram, mounted on the transducer, projects a soundfield upwards towards the surface of the water. The hologram is positioned so that its image plane is at the water-air interface. Particles travel along the resulting crests, propelled by the projected phase gradient. The motion is captured by the camera located above the surface of the water. Sizes not to scale.